AIAA JOURNAL
Vol. 48, No. 7, July 2010

Comparison of Node-Centered and Cell-Centered Unstructured Finite-Volume Discretizations: Viscous Fluxes

Boris Diskin*
National Institute of Aerospace, Hampton, Virginia 23666
James L. Thomas† and Eric J. Nielsen‡
NASA Langley Research Center, Hampton, Virginia 23681-2199
Hiroaki Nishikawa§
National Institute of Aerospace, Hampton, Virginia 23666
and
Jeffery A. White¶
NASA Langley Research Center, Hampton, Virginia 23681-2199

DOI: 10.2514/1.44940

Finite-volume discretization schemes for viscous fluxes on general grids are compared using node-centered and cell-centered approaches. The grids range from regular grids to highly irregular grids, including random perturbations of the grid nodes. Accuracy and complexity are studied for four nominally second-order accurate schemes: a node-centered scheme and three cell-centered schemes (a node-averaging scheme and two schemes using least-squares face-gradient reconstruction). The two least-squares schemes use either a nearest-neighbor or an adaptive-compact stencil at a face. The node-centered and least-squares schemes have similarly low levels of complexity. The node-averaging scheme has the highest complexity and can fail to converge to the exact solution when clipping of the node-averaged values is used. On highly anisotropic grids, typical of those encountered in grid adaptation, the least-squares schemes, the node-averaging scheme without clipping, and the node-centered scheme demonstrate similar second-order accuracies per degree of freedom. On anisotropic grids over a curved body, typical of turbulent flow simulations, the node-centered scheme is second-order accurate. The node-averaging scheme may degenerate on mixed-element grids. The least-squares schemes have to be amended to maintain second-order accuracy by either introducing a local approximate mapping or modifying the stencil to reflect the direction of strong coupling. Overall, the accuracies of the node-centered and the best cell-centered schemes are comparable at an equivalent number of degrees of freedom on isotropic and curved anisotropic grids. On stretched, randomly perturbed grids in a rectangular geometry, both gradient and discretization errors for all schemes are orders of magnitude higher than corresponding errors on regular grids.

Nomenclature

$\mathcal{A}$	=	aspect ratio
E_d	=	discretization error
E_t	=	truncation error
E_{rel}	=	relative gradient error
$\mathbf{e}_{\alpha\beta}$	=	unit vector in $[\alpha\beta]$ direction
$\mathbf{e}^{\perp}$	=	vector normal to the vector $\mathbf{e}$
f	=	forcing function
f^h	=	discrete approximation to the forcing function
h_e	=	effective mesh size, L_1 norm of $\sqrt{V}$
h_r, h_θ	=	radial and circumferential mesh spacing, respectively
h_x, h_y	=	Cartesian mesh sizes in the x and y directions, respectively
$\hat{h}_y$	=	minimal mesh spacing on stretched grids
$\{i^T\}$	=	set of nodes of cell T
$\{k_j\}$	=	set of nodes connected to node j by edges
N	=	total number of mesh points
N_x, N_y	=	number of grid points in the x and y directions, respectively
$\mathbf{n}$	=	outward-directed area vector
$\hat{\mathbf{n}}$	=	outward unit normal vector
$\check{\mathbf{n}}_i$	=	inward-directed area vector of a face opposite to node i
R	=	radius of curvature
$\mathbf{r}$	=	coordinate vector
r, θ	=	polar coordinates
s	=	distance to the designated boundary
T	=	triangle or tetrahedron
$\{T_j\}$	=	set of triangles/tetrahedra around node j
U	=	exact solution of Poisson's equation
U^h	=	discrete solution of Poisson's equation
$\overline{\nabla U}$	=	gradient of solution U evaluated by Green–Gauss formula
$\widehat{\nabla U}$	=	gradient of solution U evaluated by least-squares method
V	=	measure of a control volume
x, y	=	Cartesian coordinates
β	=	stretching factor
Γ	=	curvature-induced grid deformation parameter
Δ	=	Laplace operator
$\partial^e U$	=	edge derivative of solution U

Presented as Paper 597 at the 47th AIAA Aerospace Sciences Meeting, Orlando, FL, 5–8 January 2007; received 15 April 2009; revision received 16 February 2010; accepted for publication 17 February 2010.

*100 Exploration Way; University of Virginia, Department of Mechanical and Aerospace Engineering, Charlottesville, Virginia 22904; bdiskin@nianet.org, Senior Member AIAA.

†Computational AeroSciences Branch, Mail Stop 128; James.L.Thomas@nasa.gov. Fellow AIAA.

‡Computational AeroSciences Branch, Mail Stop 128; Eric.J.Nielsen@nasa.gov. Senior Member AIAA.

§100 Exploration Way; hiro@nianet.org. Member AIAA.

¶Computational AeroSciences Branch, Mail Stop 128; Jeffery.A.White@nasa.gov. Senior Member AIAA.

$\partial^f U$ = face derivative of solution U
θ^L, θ^R = angles between edges in two dimensions
μ = edge median
ξ, η = local coordinates
ρ = random number $\rho \in [-1, 1]$
Ω, $\partial\Omega$ = control volume and control-volume boundary, respectively
$|\cdot|$ = absolute value of a scalar or a vector
$\|\cdot\|$ = norm of interest (e.g., L_1 or L_∞)
∇ = gradient operator
∇_r = reconstructed gradient

Subscript

p = grid with perturbed nodes

Superscripts

L, R = triangles to the left and right of an edge

I. Introduction

BOTH node-centered (NC) and cell-centered (CC) finite-volume discretizations (FVDs) are widely used for complex three-dimensional (3-D) turbulent simulations in aerospace applications. The relative advantages of the two approaches have been extensively studied in the search for methods that are accurate, efficient, and robust over the broadest possible range of grid and solution parameters. The topic was discussed in a panel session at the 2007 AIAA Computational Fluid Dynamics (CFD) Conference, but a consensus did not emerge. One of the difficulties in assessing the two approaches is that comparative calculations were not completed in a controlled environment (i.e., computations were made with different codes and different degrees of freedom), and the exact solutions were not known.

In this paper, a subset of the discretization elements needed in turbulent simulations, namely that of the viscous discretization, is compared in a controlled environment. In particular, Poisson's equation is considered as a model of viscous discretization. The method of manufactured solution is used, so that the exact solution is known and smooth on the scale of the grids. Theoretical and computational studies of accuracy and complexity are conducted for a range of grids.

The two-dimensional (2-D) grids considered range from structured (regular) grids to irregular grids composed of arbitrary mixtures of triangles and quadrilaterals. Highly irregular grids are deliberately constructed through random perturbations of structured grids to bring out the worst possible behavior of the solution. Two classes of tests are considered. The first class of tests involves both isotropic and highly anisotropic grids, typical of those encountered in grid adaptation. The second class of tests involves grids varying strongly anisotropically over a curved body, typical of those encountered in high-Reynolds-number turbulent flow simulations.

Four nominally second-order accurate schemes, a NC scheme and three CC schemes, are compared for computational complexity and gradient and discretization errors at equivalent degrees of freedom. The CC schemes include a node-averaging (CC–NA) scheme and two least-squares face-gradient reconstruction schemes differing in their stencils: a nearest-neighbor (CC–NN) stencil and an adaptive-compact stencil (CC–CS). The effect of clipping is studied for the CC–NA scheme. The current version of the CC–CS scheme is derived for triangular grids, but it can be formally applied to quadrilateral and mixed-element grids, for which it is similar to the CC–NN scheme. It is expected that an effective mixed-element version of the CC–CS scheme can be derived, but it is not currently available. For the second class of tests, an approximately mapped (AM) least-squares approach is introduced to accommodate curved high-aspect-ratio grids. The mapping employs the distance function commonly available in practical codes and can be used with any scheme.

II. Grid Terminology

This paper studies FVD schemes for viscous fluxes on grids that are loosely defined as irregular. There is no commonly accepted definition for irregular grids and so, for clarity, this section specifies the grid terminology used in the paper.

A grid is classified as periodic if it has 1) a periodic node connectivity pattern (i.e., the number of edges per node changes periodically) and 2) a periodic cell distribution (i.e., the grid is composed of periodically repeated combinations of cells). Thus, periodic grids can be analyzed by Fourier analysis. Grids that are derived from periodic grids by a smooth mapping are called regular grids. Regular grids include, but are not limited to, grids derived from Cartesian ones, triangular grids obtained by diagonal splitting with a periodic pattern, smoothly stretched grids, skewed grids, smooth curvilinear grids, etc. Grids that cannot be smoothly mapped to a periodic grid are called irregular grids. Grids with varying local topology are called unstructured (e.g., grids with the number of edges changing from node to node with no pattern).

The regular and irregular grids considered in this paper are derived from an underlying (possibly mapped) Cartesian grid with mesh sizes h_x and h_y and the aspect ratio $\mathcal{A} = h_x/h_y$; both mesh sizes of the underlying grid are assumed to be small, $h_y \ll 1$ and $h_x \ll 1$. Irregularities are introduced locally and do not affect grid topology and metrics outside of a few neighboring cells. A local grid perturbation is called random if it is independent of local perturbations introduced beyond some immediate neighborhood. For computational grids generated for the reported studies, grid irregularities are introduced in two ways (both local and random): 1) the quadrilateral cells of the underlying grid are randomly split (or not split) into triangles and 2) the grid nodes are perturbed from their original positions by random shifts, taken as fractions of the local mesh size.

Four basic grid types are considered:

1) Type I consists of regular quadrilateral (i.e., mapped Cartesian) grids.

2) Type II consists of regular structured triangular grids derived from the regular quadrilateral grids by the same diagonal splitting of each quadrilateral.

3) Type III consists of random triangular grids, in which regular quadrilaterals are split by randomly chosen diagonals, each diagonal orientation occurring with a probability of half.

4) Type IV consists of random mixed-element grids, in which regular quadrilaterals are randomly split or not split by randomly chosen diagonals, the probabilities of splitting and of choosing a particular diagonal are half.

Grids of types III–IV are irregular and unstructured because there is no periodic connectivity pattern. Nodes of any basic-type grid can be perturbed from their initial positions by random shifts, thus leading to four additional perturbed grid types that are designated by subscript p as I_p–IV_p. All perturbed grids are irregular, because there is no periodic cell distribution. The representative grids are shown in Fig. 1.

Our main interest is the accuracy and complexity of FVD schemes on general irregular grids with a minimum set of constraints. In particular, grid smoothness is not required, neither on individual grids nor in the limit of grid refinement. The only major requirement for a sequence of refined grids is to satisfy the consistent refinement property. This property requires the maximum distance across the grid cells to decrease consistently with the increase of the total number of grid points, N. In particular, the maximum distance should tend to zero as $N^{-1/2}$ in 2-D computations. For 3-D unstructured grids, the consistent refinement property is studied in [1]. On 2-D grids, the effective mesh size h_e is computed as the L_1 norm of the square root of the control volumes.

The locations of discrete solutions are called data points. For consistency with the 3-D terminology, the 2-D cell boundaries are called faces, and the term edge refers to a line (possibly virtual) connecting the neighboring data points. Each face is characterized by two vectors: 1) the edge vector, which connects the data points of the cells sharing the face and 2) the directed-area vector, which is normal

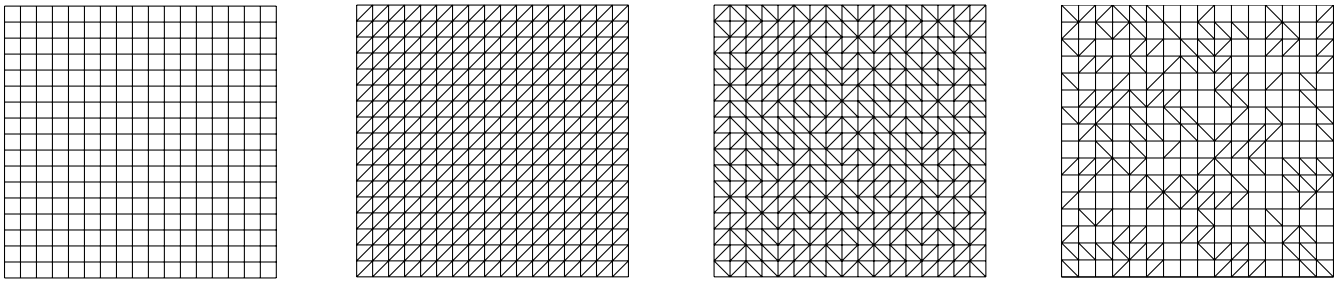

a) Type *I*: regular quadrilateral grid

b) Type *II*: regular structured triangular grid

c) Type *III*: random triangular grid

d) Type *IV*: random mixed grid

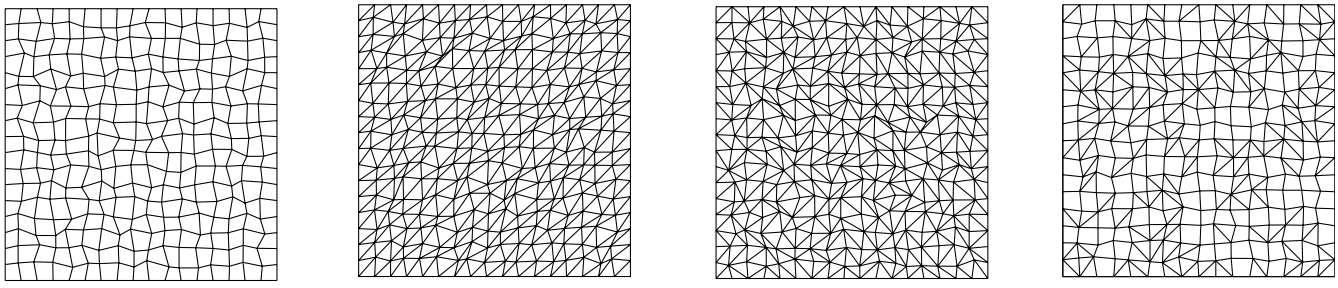

e) Type I_p: perturbed quadrilateral grid

f) Type II_p: perturbed structured triangular grid

g) Type III_p: perturbed random triangular grid

h) Type IV_p: perturbed random mixed grid

Fig. 1 Grids: a) and b) typical regular, and c)–h) irregular.

to the face with magnitude equal to the face area. For each cell/face combination, the vectors are directed outward.

For grids of types I_p–IV_p, the random node perturbation in each dimension is defined as $\frac{1}{4}\rho h$, where $\rho \in [-1,\ 1]$ is a random number, and h is the local mesh size along the given dimension. With these perturbations, triangular cells in the rectangular geometry can approach zero volume. The random perturbations are introduced independently on all grids, implying that on grids of types I_p–IV_p, the ratios of neighboring cell volumes and face areas are random and do not approach unity in the limit of grid refinement.

III. Finite-Volume Discretization Schemes

The considered model problem is Poisson's equation,

$$\Delta U = f \tag{1}$$

subject to Dirichlet boundary conditions, where function f is a forcing function. The 2-D primal meshes generated for this study are composed of triangular and quadrilateral cells. The FVD schemes are derived from the integral conservation law,

$$\oint_{\partial\Omega} \nabla U \cdot \hat{\mathbf{n}}\ \mathrm{d}s = \int_{\Omega} f\,\mathrm{d}\Omega \tag{2}$$

where ∇U is the solution gradient, Ω is a control volume with boundary $\partial\Omega$, and $\hat{\mathbf{n}}$ is the outward unit normal vector. The general FVD approach requires partitioning the domain into a set of nonoverlapping control volumes and numerically implementing Eq. (2) over each control volume.

CC discretizations assume solutions are defined at the centers of the primal-grid cells, with the primal cells serving as the control volumes. The cell center is typically defined as the average of the vortices defining the cell (i.e., not necessarily a centroid). NC discretizations assume solutions are defined at the primal-mesh nodes. For NC schemes, control volumes are constructed around the mesh nodes by the median-dual partition: the centers of primal cells are connected with the midpoints of the surrounding faces. These nonoverlapping control volumes cover the entire computational domain and compose a mesh that is dual to the primal mesh. Both CC and NC control-volume partitions are illustrated in Fig. 2.

A. Cell-Centered Finite-Volume Discretization Schemes

In CC discretizations, the conservation law in Eq. (2) is enforced on control volumes that are primary cells. The flux at a face is computed as the inner product of the solution gradient at the face and the directed-area vector. The at-face solution gradient is typically reconstructed from the solution values at the neighboring cells and augmented with the edge-directional gradient. Augmentation is used to decrease the scheme susceptibility to odd–even decoupling [2,3]. Two possible augmentation strategies, edge normal and face tangent, are discussed in [2,4]. In this paper, the face-tangent augmentation strategy is implemented for CC schemes. The schematic of the face-tangent gradient augmentation is illustrated in Fig. 3.

With reference to Fig. 2, the gradient, $\nabla_r U_{04}$ (at the face-linking nodes 0 and 4) is computed as

$$\nabla_r U_{04} = \frac{1}{\hat{\mathbf{n}}\cdot\hat{\mathbf{e}}}\,\partial^e U\hat{\mathbf{n}} + \partial^f U\left[\hat{\mathbf{f}} - \frac{\hat{\mathbf{f}}\cdot\hat{\mathbf{e}}}{\hat{\mathbf{n}}\cdot\hat{\mathbf{e}}}\,\hat{\mathbf{n}}\right] \tag{3}$$

Here,

$$\hat{\mathbf{e}} = (\mathbf{r}_B - \mathbf{r}_A)/|\mathbf{r}_B - \mathbf{r}_A| \tag{4}$$

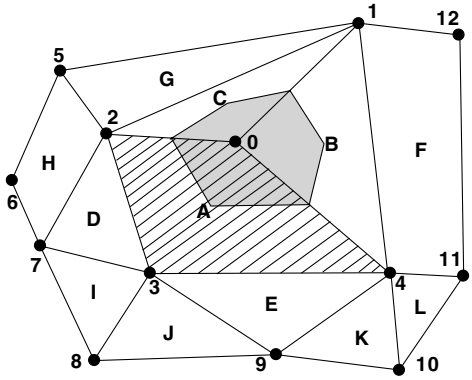

Fig. 2 Control-volume partitions for FVDs. Numbers 0–12 and letters A–L denote grid nodes and primal cell centers, respectively. The control volume for a NC discretization around grid node 0 is shaded. The control volume for a CC discretization around the cell center *A* is hashed.

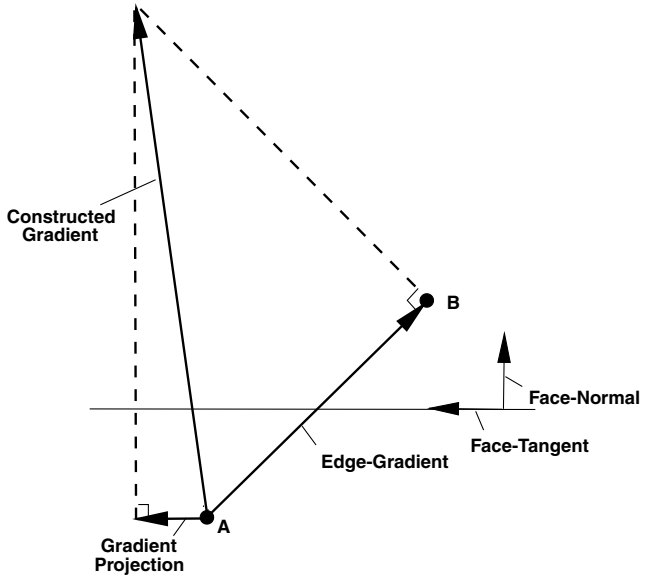

Fig. 3 Face-tangent gradient augmentation; gradient projection is $\partial^f U\hat{\mathbf{f}}$.

is the unit vector aligned with the virtual edge $[A,\ B]$, $\mathbf{r}_A$ and $\mathbf{r}_B$ are the cell-center coordinate vectors, $\hat{\mathbf{n}}$ is the unit vector normal to the control-volume face $[0, 4]$ directed outward from cell center A,

$$\hat{\mathbf{f}} = (\mathbf{r}_0 - \mathbf{r}_4)/|\mathbf{r}_0 - \mathbf{r}_4| \tag{5}$$

is a unit vector normal to $\hat{\mathbf{n}}$,

$$\partial^e U = \frac{U_B - U_A}{|\mathbf{r}_B - \mathbf{r}_A|} \tag{6}$$

is the edge-directional derivative, and $\partial^f U$ is the solution derivative computed along the face $[0, 4]$.

The face-tangent augmentation enforces that $\nabla_r U_{04}$ recovers: 1) the edge-directional derivative,

$$\nabla_r U_{04} \cdot \hat{\mathbf{e}} = \partial^e U \tag{7}$$

and 2) the face-tangent derivative,

$$\nabla_r U_{04} \cdot \hat{\mathbf{f}} = \partial^f U \tag{8}$$

The CC FVD schemes considered in this paper differ only in computing $\partial^f U$.

1. Node-Averaging Face Gradient

In the CC–NA schemes, the solution derivative along the face, $\partial^f U$, is computed as the divided difference between the solution values reconstructed at the nodes from the surrounding cell centers. With respect to Fig. 2, the solution at node 0 is reconstructed by averaging solutions defined at the cell centers A, B, and C. The solution reconstruction proposed in [5,6] and used in [7] is an averaging procedure that is based on a constrained optimization to satisfy some Laplacian properties. The scheme is second-order accurate and stable when the coefficients of the introduced pseudo-Laplacian operator are close to one. It has been shown in [8] that this averaging procedure is equivalent to an unweighted least-squares linear fit. For the face $[0, 4]$,

$$\partial^f U = \frac{\hat{U}_0 - \hat{U}_4}{|\mathbf{r}_0 - \mathbf{r}_4|} \tag{9}$$

where $\hat{U}_i$ and $\mathbf{r}_i$ are the averaged solution and the coordinate vector of the node i.

On highly stretched and deformed grids, some coefficients of the pseudo-Laplacian may become negative or larger than two, which has a detrimental effect on stability and robustness [9,10]. Holmes and Connell [5] proposed to enforce stability by clipping the coefficients between 0 and 2. The CC–NA schemes with clipping represent a current standard in practical CFD for applications involving CC finite-volume formulations [11]. As shown further in the paper, clipping seriously degrades the solution accuracy.

2. Least-Squares Scheme Face Gradient

An alternative CC scheme relies on a face-based least-squares method. First, an auxiliary face gradient $\widehat{\nabla U}$ is reconstructed within a face using a least-squares procedure. Then, the derivative along the face is computed as

$$\partial^f U = \widehat{\nabla U} \cdot \hat{\mathbf{f}} \tag{10}$$

The two approaches to determine stencils for the least-squares linear fit at a face are described as follows. The CC–NN six-point stencil consists of the two prime cells sharing the face and their face neighbors, which share one of the face nodes. In Fig. 4a, the CC–NN stencil for the highlighted face is denoted by circles.

The CC–CS is important for discretizations on high-aspect-ratio grids of types II and III to correctly represent the direction of the strong coupling. It is constructed by choosing between two stencils for face least-squares gradient reconstruction: a six-point stencil and a minimal (typically four-point) stencil. In general, the minimal stencil takes advantage of the local topology associated with grids generated with advancing layer methods, and it is intended for long faces of high-aspect-ratio triangular grids.

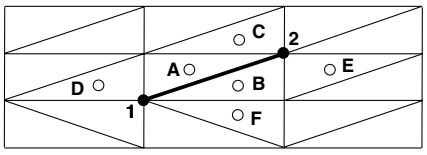

a) Face least-squares stencil with CC-NN scheme

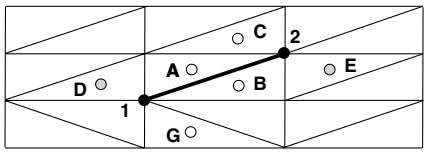

b) Face least-squares stencil with CC-CS scheme

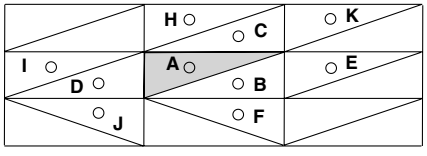

c) Laplacian stencil for the shaded cell with CC-NN scheme

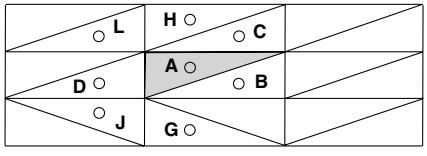

d) Laplacian stencil for the shaded cell with CC-CS scheme

Fig. 4 Stencils on high-aspect-ratio grids of type III. Figures are vertically expanded for better visualization.

Specifically, at each face, the CC–CS method first attempts to construct a six-point stencil by combining two prime cells and four auxiliary cells; each auxiliary cell is associated with a prime cell and a face node. The method chooses the auxiliary cell that 1) shares the face node, 2) is located on the opposite side of the face from the associated prime cell center, 3) is not already in the stencil, and 4) has the shortest distance to the center of the associated prime cell. The six-point stencil for the highlighted diagonal face is denoted by the union of empty and filled circles in Fig. 4b. Note that cell F in the CC–NN stencil (Fig. 4a) is replaced by cell G in the six-point CC–CS stencil. For the prime cell A on high-aspect-ratio grids, the nearest cell that shares node 1 and is on the opposite side of the face [1, 2] is cell$G$, not cell$F$. In the process of construction, the closest auxiliary cell associated with each primal cell is identified. The minimal stencil is defined by the union of the prime cells and their closest associated auxiliary cells. In Fig. 4b, cell G is the closest auxiliary cell to the primal cell A, cell C is the closest auxiliary cell to the primal cell B, and the minimal stencil is shown as empty circles. Note that, in some local geometries, a prime cell may have no auxiliary cells. In such cases, the minimal stencil consists of less than four points.

The CC–CS method selects the minimal stencil if either the six-point stencil cannot be formed following the rules 1–4 (which may happen next to the boundaries or in curved geometries) or the minimal stencil represents an ideal four-point pairwise construction. The four-point pairwise construction is considered ideal if one can form two pairs, with each pair satisfying the three following geometrical conditions. The data points within the pair 1) are on opposite sides of the face, 2) are closer than a predefined threshold (typically taken as a fraction of the larger local mesh size), and 3) have a skew angle (the angle between the vector connecting the points and the face directed-area vector) smaller than a predefined threshold. For computations on high-aspect-ratio grids, the distance threshold has been chosen as $\frac{3}{16}h_x$, where h_x is the larger mesh size of the background Cartesian grid, and the skew threshold has been chosen as $\sin^{-1}(0.1)$. The four-point stencil in Fig. 4b is considered ideal.

Figures 4c and 4d compare CC–NN and CC–CS stencils corresponding to the FVD of Poisson's equation on the shaded cell. The CC–CS scheme uses minimal stencils for diagonal and horizontal faces and a six-point stencil for vertical faces. The CC–CS stencil is more compact than the CC–NN stencil and provides a three-point vertical structure centered at the shaded cell center that better reflects the grid anisotropy direction.

Remark: It is known that on high-aspect-ratio curved grids, unweighted least-squares methods have difficulties with reconstructing accurate gradients within a cell [12–14]. Inverse distance weighting has been shown to improve gradient accuracy. For face-centered least-squares reconstruction, the usual weightings (with distances measured from the face center) do not improve gradient accuracy, because all points involved in least-squares stencils are typically at comparable distances from the face center. A modified weighting, which is based on minimal distances from the two cell centers across the face, with an extended stencil (the stencil that is used in CC–NA scheme) improves gradient accuracy on high-aspect-ratio curved grids derived by an advanced-layer method. The weighting effectively reduces the extended stencil to the minimal stencil of the CC–CS scheme. However, the method led to unstable formulations on general irregular grids and was not pursued further.

B. Node-Centered Finite-Volume Discretization Scheme

The second-order accurate NC FVD scheme illustrated by Fig. 5 represents a standard CFD approach to NC viscous discretizations. The scheme approximates the integral flux through the dual faces adjacent to the edge [0, 4] as

$$\int_{A\mu B} \nabla U \cdot \hat{\mathbf{n}}\, \mathrm{d}s \approx \nabla_r U_{A\mu} \cdot \mathbf{n}_{A\mu} + \nabla_r U_{\mu B} \cdot \mathbf{n}_{\mu B} \tag{11}$$

where μ is the median of the edge [0, 4]. The gradient is reconstructed separately at each dual face as follows.

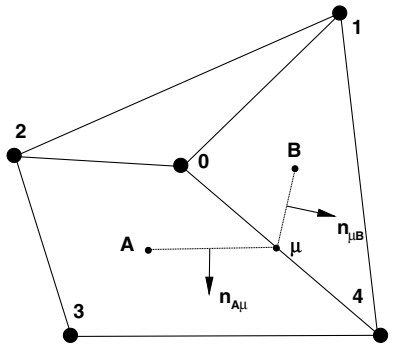

Fig. 5 Illustration of gradient reconstruction for viscous terms on mixed grids with median-dual partition.

For the triangular element contribution, the gradient is determined from a Green–Gauss evaluation at the primal-grid element:

$$\nabla_r U_{\mu B} = \overline{\nabla U}_{014} \tag{12}$$

The gradient overbar denotes a gradient evaluated by the Green–Gauss formula on the primal cell identified by the point subscripts. With fully triangular elements, the formulation is equivalent to a Galerkin finite-element scheme with a linear basis function [9,15]. Analysis in Appendix A shows that on unperturbed triangular grids of types II and III in rectangular geometries, the formulation recovers the five-point Laplacian stencil of the type I grids, independent of aspect ratio.

For the quadrilateral element contribution, the gradient $\nabla_r U_{A\mu}$ is constructed as the Green–Gauss gradient augmented with the edge derivative,

$$\nabla_r U_{A\mu} = \overline{\nabla U}_{0234} + [\partial^e U - \overline{\nabla U}_{0234} \cdot \mathbf{e}_{04}]\mathbf{e}_{04} \tag{13}$$

where

$$\partial^e U = \frac{U_4 - U_0}{|\mathbf{r}_4 - \mathbf{r}_0|} \tag{14}$$

is the edge derivative, U_i is the solution at node i, and

$$\mathbf{e}_{04} = \frac{\mathbf{r}_4 - \mathbf{r}_0}{|\mathbf{r}_4 - \mathbf{r}_0|} \tag{15}$$

is the unit vector aligned with the edge [0, 4]. The edge-normal augmentation illustrated in Fig. 6 is used to enforce that the constructed gradient recovers 1) the edge-directional derivative,

$$\nabla_r U_{A\mu} \cdot \mathbf{e}_{04} = \partial^e U \tag{16}$$

and 2) the Green–Gauss gradient projected on the direction normal to $\mathbf{e}_{04}$:

$$\nabla_r U_{A\mu} \cdot \mathbf{e}_{04}^{\perp} = \overline{\nabla U}_{0234} \cdot \mathbf{e}_{04}^{\perp} \tag{17}$$

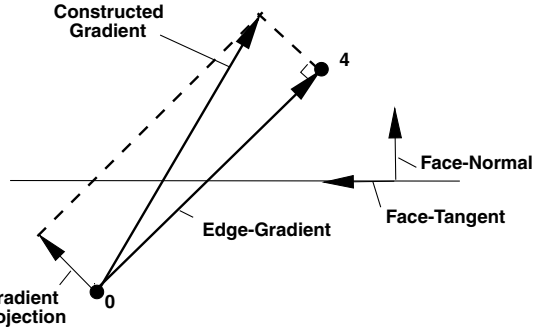

Fig. 6 Edge-normal gradient augmentation; gradient projection is $\overline{\nabla U} - (\overline{\nabla U} \cdot \mathbf{e})\mathbf{e}$.

Note that, for grids with dual faces perpendicular to the edges, the edge gradient $\partial^e U$ is the only contributor. It has been shown [1,16] that the scheme possesses second-order accuracy for viscous fluxes on general isotropic mixed-element grids.

IV. Complexity of Discretization Stencils

The size of the stencil for the viscous discretization is examined for 2-D and 3-D CC and NC FVD schemes. Estimates are made for Cartesian meshes split into triangular and tetrahedral elements, neglecting any boundary effects.

In 2-D, two splittings of the Cartesian grid are considered. The first splits each quadrilateral cell with a diagonal oriented in the same direction. The second splits the cells with diagonals of face-adjacent quadrilaterals oriented in the opposite direction. The second splitting is slightly more analogous to the 3-D splitting. In 3-D, half of the grid nodes have 18 incident edges (32 incident tetrahedra) and half have six incident edges (eight incident tetrahedra). Each of the tetrahedra interior to an originally hexahedral cell is defined by four nodes, each with 18 incident edges. Each of the four surrounding tetrahedra within an originally hexahedral cell is defined by three nodes with 18 incident edges and one node with six incident edges.

Table 1 shows stencil-size estimates for triangular/tetrahedral grids and a numerical calculation on an actual 3-D turbulent viscous grid that includes boundary effects. There is a slight difference in the 2-D estimates from the two splittings (entries separated by slashes in the table), depending on the diagonalization pattern. The CC–NA stencil is the largest. The CC–NN stencil is only slightly larger than the stencil of the NC discretization, in both estimation and computation. The complexity of the CC–CS stencil is even smaller.

V. Analysis Methods

The accuracy of FVD schemes is analyzed for known exact or manufactured solutions. The forcing function and boundary values are found by substituting this solution into the Poisson equation with Dirichlet boundary conditions. The discrete forcing function is defined at the data points.

A. Discretization Error

The main accuracy measure is the discretization error E_d, which is defined as the difference between the exact discrete solution U^h of the discretized Eq. (2) and the exact continuous solution U to the differential Eq. (1),

$$E_d = U - U^h \tag{18}$$

where U is sampled at the data points.

B. Truncation Error

Another accuracy measure commonly used in computations is truncation error. Truncation error E_t characterizes the accuracy of approximating the differential equation (1). For finite differences, it is defined as the residual obtained after substituting the exact solution U into the discretized differential equations [17]. For FVD schemes, the traditional truncation error is usually defined from the time-dependent standpoint [18,19]. In the steady-state limit, it is defined (e.g., in [20]) as the residual computed after substituting U into the normalized discrete Eq. (2),

Table 1 Average size of the viscous stencil on triangular (2-D) and tetrahedral (3-D) grids. The two numbers for CC 2-D schemes correspond to different diagonalization patterns

	NC	CC–NA	CC–NN
2-D estimate	7	13/16	10/9
3-D estimate	13	79	15
3-D numerical	14	69	15

$$E_t = \frac{1}{V}\left[-\int_\Omega f^h \, \mathrm{d}\Omega + \oint_{\partial\Omega} (\nabla_r U \cdot \hat{\mathbf{n}}) \, \mathrm{d}s \right] \tag{19}$$

where V is the measure of the control volume,

$$V = \int_\Omega \mathrm{d}\Omega \tag{20}$$

f^h is an approximation of the forcing function f on Ω, and the integrals are computed according to some quadrature formulas. Note that convergence of truncation errors is expected to show the order property only on regular grids. It has been long known that, on irregular grids, the design-order discretization-error convergence can be achieved. even when truncation errors exhibit a lower-order convergence or, in some cases, do not converge at all [21–23].

C. Accuracy of Gradient Reconstruction

Yet another important accuracy measure is the accuracy of gradient approximation at a control-volume face. For second-order convergence of discretization errors, the gradient is usually required to be approximated with at least first order. For each face, accuracy of the gradient is evaluated by comparing the reconstructed gradient $\nabla_r U$ with the exact gradient ∇U computed at the face center. The gradient reconstruction uses a discrete representation (usually injection) of the exact solution U at data points on a given grid. The accuracy of gradient reconstruction is measured as the relative gradient error,

$$E_{\mathrm{rel}} = \frac{\|\epsilon\|}{\|G\|} \tag{21}$$

where functions ϵ and G define at-face magnitudes of the gradient error and the exact gradient, respectively,

$$\epsilon = |\nabla_r U - \nabla U| \tag{22}$$

and

$$G = |\nabla U|$$

and $\|\cdot\|$ is a norm of interest computed over the entire computational domain. For the NC scheme, the exact and reconstructed gradients are evaluated at the centers of primal cells.

VI. Isotropic Irregular Grids

A. Grid Refinement

A sequence of consistently refined grids of type III_p is generated on the unit square $[0,\ 1] \times [0,\ 1]$. Irregularities are introduced at each grid independently. The ratio of areas of neighboring faces can be as large as $3\sqrt{2}$. The ratio of the neighboring volumes can be arbitrarily high, because a control volume can be arbitrarily small. Isotropic grids randomly generated for this study have 0.01% of cell volumes smaller than $\frac{1}{10}\frac{1}{N}$, where N is the total number of grids nodes.

B. Gradient Reconstruction Accuracy

The accuracy of gradient reconstruction for isotropic irregular grids is first order for all methods [24], which is sufficient for second-order discretization accuracy. As an example, the gradient reconstruction tests are performed for the manufactured solution $U = \sin(\pi x + 2\pi y)$. Figure 7 shows convergence of the L_∞ norms of relative gradient errors computed on a sequence of refined grids of type III_p. All methods provide first-order gradient approximations and very similar relative errors. Note that, because the gradients of the NC scheme are evaluated at the primal cell centers, the effective mesh size of gradient reconstruction is the same for all schemes.

C. Convergence of Truncation and Discretization Error

The numerical tests evaluating convergence of truncation and discretization errors are performed with Dirichlet boundary conditions specified from the manufactured solution $U = \sin(\pi x + 2\pi y)$.

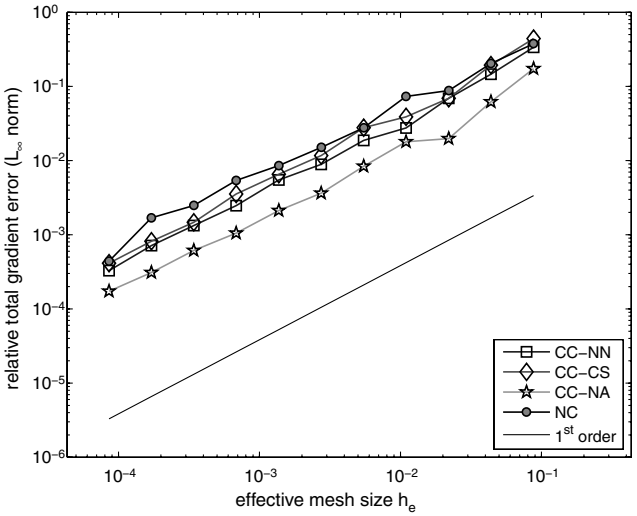

Fig. 7 Accuracy of gradient reconstruction on isotropic irregular grids of type III$_p$.

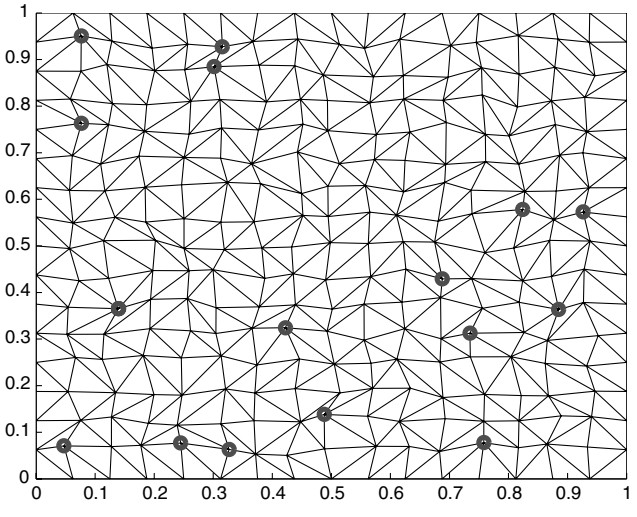

a) Random triangular grid with 17^2 nodes. Clipped nodes are circled

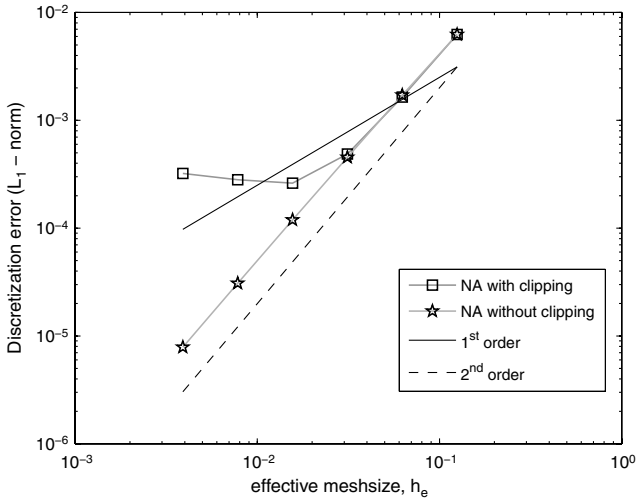

b) Discretization errors

Fig. 9 Accuracy of CC–NA schemes on isotropic irregular triangular grids of type III$_p$.

For CC formulations, the solution is specified on all cells linked to the boundary. Figure 8 shows convergence of the L_1 norms of truncation and discretization errors for the NC and two CC formulations on grids of type III$_p$. As predicted in [1,16], truncation errors do not converge on irregular grids in any norm. Discretization errors converge with second order for all formulations considered. The discretization errors of the CC and NC FVD schemes are almost overplotted, indicating a similar accuracy per degree of freedom. Note that a given multidimensional grid typically has more primal cells than nodes. Thus, on a given grid, a CC scheme has more degrees of freedom than a NC scheme and, consequently, is expected to have a better accuracy.

D. Effects of Clipping

The tests reported in this section are performed for the CC–NA schemes and demonstrate detrimental effects of clipping on accuracy of gradient approximation and on the discretization accuracy. The accuracy is evaluated for the manufactured solution $U = \sin(2\pi y)$. Considered irregular grids of type III$_p$ are derived from underlying isotropic (unit aspect ratio) Cartesian grids covering the unit square. Figure 9a shows an example of an isotropic random triangular grid of type III$_p$ with 17^2 nodes. About 7% of the interior nodes are clipped.

It has been demonstrated in [25] that the face gradients computed by the CC–NA scheme with clipping do not approximate the exact gradients on grids of type III$_p$. The normal and tangential components of the computed gradients were evaluated within interior faces and compared with the exact gradient components at the face center. The maximum norms of the deviations between the computed and the exact gradient components did not converge in grid refinement. The CC–NA scheme without clipping provided a first-order-accurate

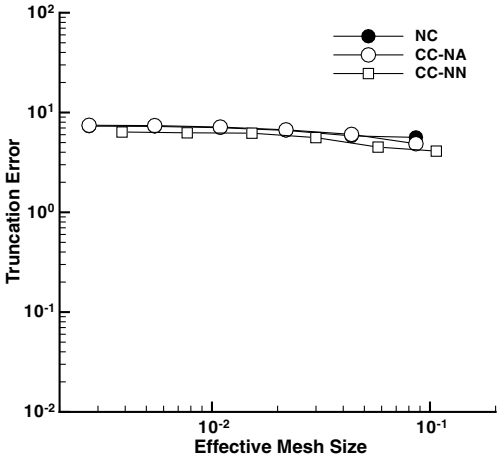

a) Truncation Errors

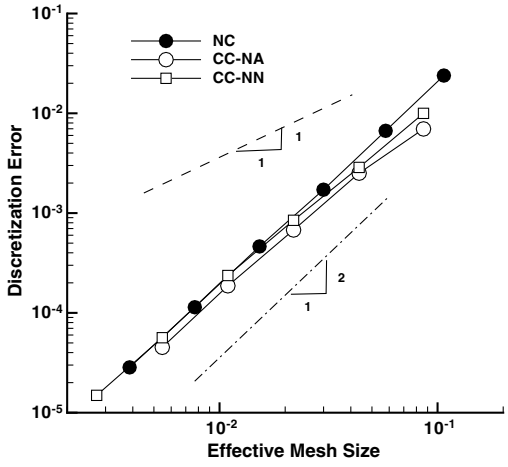

b) Discretization Errors

Fig. 8 Convergence of L_1 norms of truncation and discretization errors on random triangular grids of type III$_p$.

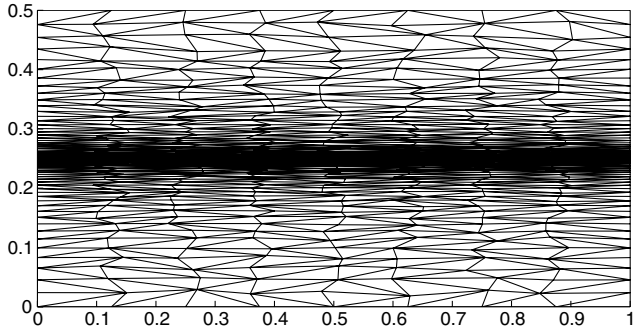

Fig. 10 Stretched grid of type III$_p$ with 9 × 65 nodes.

gradient approximation. Figure 9b exhibits convergence of the L_1 norms of discretization errors. Although the CC–NA scheme without clipping demonstrates second-order convergence on all grids, convergence of the CC–NA scheme with clipping degrades to zeroth order on finer grids. Although not shown, the L_∞ norms of the discretization errors converge with the same orders as the corresponding L_1 norms.

VII. Anisotropic Grids

This section considers FVD schemes on irregular stretched grids generated on rectangular domains. Figure 10 shows an example grid with the maximal aspect ratio $\mathcal{A} = 1000$. A sequence of consistently refined stretched grids is generated on the rectangle $(x, y) \in [0, 1] \times [0, 0.5]$ in the following three steps.

1) A background regular rectangular grid with $N = (N_x + 1) \times (N_y + 1)$ nodes and the horizontal mesh spacing $h_x = 1/N_x$ is stretched toward the horizontal line $y = 0.25$. The y coordinates of the horizontal grid lines in the top half of the domain are defined as

$$y_{(N_y/1)+1} = 0.25; \qquad y_j = y_{j-1} + \hat{h}_y \beta^{j-[(N_y/2)+1)]};$$
$$j = \frac{N_y}{2} + 2, \ \ldots, \ N_y, \ N_y + 1 \tag{23}$$

Here, $\hat{h}_y = h_x/A$ is the minimal mesh spacing between the vertical lines, $\mathcal{A} = 1000$ is a fixed maximal aspect ratio, and β is a stretching factor that is found from the condition $y_{N_y+1} = 1$. The stretching in the bottom half of the domain is defined analogously.

2) Irregularities are introduced by random shifts of interior nodes in the vertical and horizontal directions. The vertical shift is defined as $\Delta y_j = \frac{3}{16}\rho \min(h_y^{j-1}, h_y^j)$, where ρ is a random number between -1 and 1, and h_y^{j-1} and h_y^j are vertical mesh spacings on the background stretched mesh around the grid node. The horizontal shift is introduced analogously, $\Delta x_i = \frac{3}{16}\rho h_x$. With these random node perturbations, all perturbed quadrilateral cells are convex.

3. Each perturbed quadrilateral is randomly triangulated with one of the two diagonal choices; each choice occurs with a probability of one half.

A recent study [24] assessed the accuracy of gradient approximation on various irregular grids with a high aspect ratio of $\mathcal{A} = h_y/h_x \gg 1$. The study indicates that, for rectangular geometries and functions predominantly varying in the direction of small mesh spacing (y direction), gradient reconstruction is accurate. For manufactured solutions significantly varying in the direction of larger mesh spacing (x direction), the face-gradient reconstruction may produce extremely large $O(\mathcal{A}h_x)$ relative errors affecting the accuracy of the y-directional gradient component. Figures 11a and 11b confirm this analysis and show examples of gradient approximations that exhibit first-order accuracy and large relative errors on high-aspect-ratio grids of type III. On these grids, the NC scheme and CC–CS scheme produce accurate gradients for all solutions, independent of grid aspect ratio. Accuracy of gradients reconstructed with CC–NN and CC–NA schemes is directly proportional to $\mathcal{A}h_x$ and typically poor for solutions varying in the x direction of larger mesh spacing, unless the grids are extremely fine. For solutions varying predominantly in the y direction of smaller mesh spacing, all schemes produce accurate gradients.

A summary of the previous results [24] for grids of all types (supplemented by the results for the CC–CS scheme) is presented in Table 2. All considered gradient reconstruction methods are accurate on regular quadrilateral grids of type I, but they may generate large relative errors on irregular grids of types I$_p$–IV$_p$ with perturbed nodes. The CC–NA and CC–NN methods may also have large relative errors on unperturbed grids of types II–IV. The CC–CS gradients are accurate for unperturbed triangular grids; the accuracy of CC–CS gradients is similar to the accuracy of the CC–NN gradients on mixed-element grids of type IV. The NC method using the Green–Gauss approach always provides accurate gradients on unperturbed grids.

However, a poor gradient reconstruction accuracy does not necessarily imply a large discretization error. Mavriplis [12] reported (second-order) accurate NC solutions, even on grids with large gradient reconstruction errors. Here, similar results are observed for CC and NC formulations.

Sequences of consistently refined stretched grids with a maximum aspect ratio of $\mathcal{A} = 1000$, including 9×65, 17×129, 33×257, and 65×513 nodes have been considered. The corresponding stretching ratios are $\beta \approx 1.207$, 1.098, 1.048, and 1.025. The grids of types III and III$_p$ are representative for general perturbed and unperturbed grids, respectively. Convergence of the L_1 norms of discretization

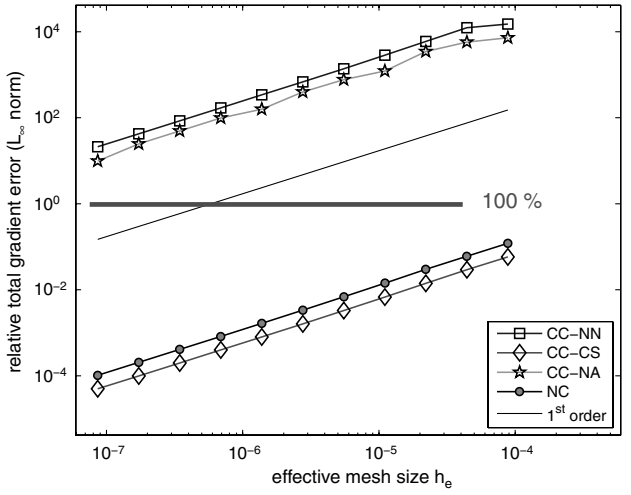

a) $U = \sin(\pi x + 2\pi y)$; $\mathcal{A} = 10^6$

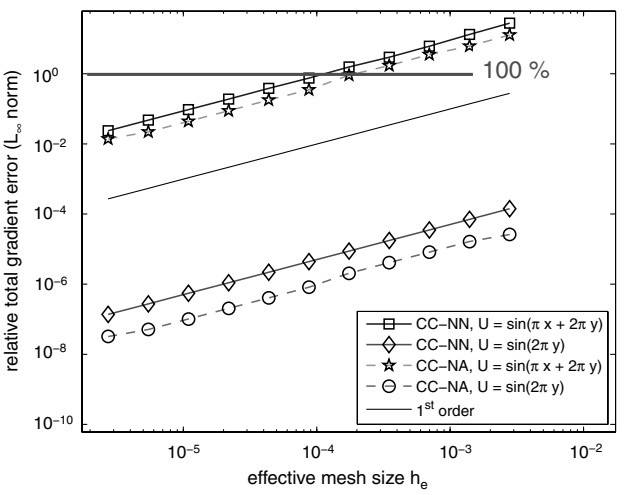

b) $U = \sin(\pi x + 2\pi y)$ and $U = \sin(2\pi y)$, $\mathcal{A} = 10^3$

Fig. 11 Relative errors in approximation of face gradients on anisotropic grids of type III.

Table 2 Relative error of gradient reconstruction on anisotropic grids in rectangular domains

Grids	I	II	III	IV	I_p–IV_p
NC	$O(h_x^2)$	$O(h_x)$	$O(h_x)$	$O(h_x)$	$O(\mathcal{A}h_x)$
CC–NA	$O(h_x^2)$	$O(\mathcal{A}h_x^2)$	$O(\mathcal{A}h_x)$	$O(\mathcal{A}h_x)$	$O(\mathcal{A}h_x)$
CC–NN	$O(h_x^2)$	$O(\mathcal{A}h_x^2)$	$O(\mathcal{A}h_x)$	$O(\mathcal{A}h_x)$	$O(\mathcal{A}h_x)$
CC–CS	$O(h_x^2)$	$O(h_x^2)$	$O(h_x)$	$O(\mathcal{A}h_x)$	$O(\mathcal{A}h_x)$

errors for the manufactured solution $U = \cos(\pi x + 2\pi y)$ is shown in Fig. 12. The highly stretched grids are not well suited with the manufactured solution, but such a mismatch is chosen intentionally to demonstrate convergence in the worst-case scenario.

All tests have been performed stochastically [i.e., multiple grids (ten)] with different irregularities; patterns have been independently generated on each scale (same number of nodes). The plot symbols indicate the mean errors, and the bars indicate the maximum and minimum errors observed on each scale. The effective mesh size is practically the same for all CC schemes at a given scale, but for visualization purposes, plots of the CC–NA and CC–CS schemes are shifted to the right and the left, respectively, of the CC–NN scheme.

All discretization errors are relatively small and converge with second order. The errors on grids of type III are about two orders of magnitude smaller than the errors on the grids of type III_p. The NC scheme is remarkably insensitive to grid irregularities on all grids. Large variations of discretization errors are observed for CC schemes on coarse grids of type III_p. The largest variation is with the CC–NN scheme. Error variations for all schemes are decreasing on finer scales. On grids of type III, the error variations are small on all scales. The CC schemes tend to show smaller errors on coarser grids, but they require finer grids to establish the second-order convergence. Although not shown, on grids of type III_p, the level of errors for the solution $U = \cos(2\pi y)$ varying only in the y direction is more than two orders of magnitude smaller than the level of errors for the solution $U = \cos(\pi x + 2\pi y)$ that has a significant variation in the x direction.

VIII. Grids with Curvature and High-Aspect Ratio

This section discusses the accuracy of FVD schemes on grids with large deformations induced by a combination of curvature and a high aspect ratio. Grids of types I–IV are considered for the cylindrical geometry. Random node perturbation is not applied, because even small perturbations in the circumferential direction may lead to nonphysical control volumes. Representative stretched grids of types III and IV are shown in Fig. 13. The grid nodes are generated from a cylindrical mapping, where (r, θ) denotes polar coordinates with spacings of h_r and h_θ, respectively. The innermost radius is $r = R$. The grid aspect ratio is defined as the ratio of mesh sizes in the circumferential and the radial directions, $\mathcal{A} = Rh_\theta/h_r$. The mesh deformation is characterized by the parameter Γ:

$$\Gamma = \frac{R[1 - \cos(h_\theta)]}{h_r} \approx \frac{Rh_\theta^2}{2h_r} = \mathcal{A}\frac{h_\theta}{2} \tag{24}$$

The following assumptions are made about the range of parameters: $R \approx 1$, $\mathcal{A} \gg 1$, and $\Gamma h_r \ll 1$, which implies that both h_r and h_θ are small. For a given value of $\mathcal{A}$, the parameter Γ may vary: $\Gamma \gg 1$ corresponds to meshes with large curvature-induced deformation, and $\Gamma \ll 1$ indicates meshes that are locally (almost) Cartesian. In a mesh refinement that keeps $\mathcal{A}$ fixed, $\Gamma = O(\mathcal{A}h_\theta)$ asymptotes to zero. This property implies that, on fine enough grids with a fixed curvature and an aspect ratio, the discretization-error convergence is expected to be the same as on similar grids generated on rectangular domains with no curvature.

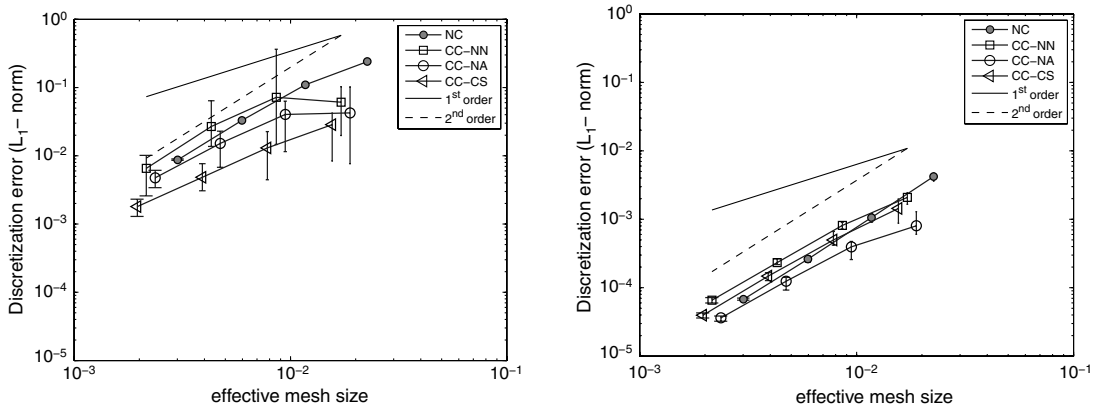

a) Type *III*$_p$ **b) Type *III***

Fig. 12 Convergence of discretization errors for solution $U = \cos(\pi x + 2\pi y)$ on stretched grids with a maximum aspect ratio of $\mathcal{A} = 1000$.

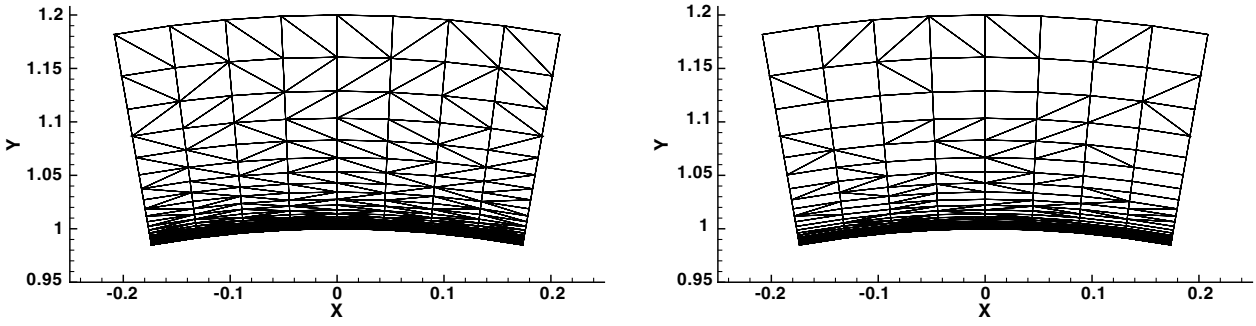

a) Grid of type *III* **b) Grid of type *IV***

Fig. 13 Representative 9 × 33 stretched high-Γ grids.

The focus in this section is on convergence of discretization errors on high-Γ grids with large curvature-induced deformations, following a previous study [24] that focused on gradient accuracy. The considered manufactured solutions predominantly vary in the radial direction of small mesh spacing.

A. Accuracy of Gradient Approximation

Gradient approximation accuracy on deformed grids with high Γ has been studied in the literature, mostly in regard to NC discretizations of inviscid terms [12–14]. The observations and analysis indicated that the unweighted least-squares methods poorly approximate gradients at control-volume centers. The main reasons for poor gradient approximation are 1) the stencil deformation and 2) heavy reliance of the unweighted least-squares method on solutions at distant points. Weighted least-squares methods have been proposed to reduce the effect of distant points and, thus, to improve gradient accuracy.

The situation is different for the viscous terms, for which the gradient reconstruction is required at the control-volume face, not at the center. The gradients of the NC scheme and the gradients of the CC–CS scheme on triangular grids use the minimal stencil and are expected to be accurate on unperturbed grids, independent of aspect ratio. For other CC schemes, the at-face gradient reconstruction is more difficult. The more extended stencils of least-squares methods involved either in CC–NA or in CC–NN gradient reconstruction are significantly deformed, and reconstructions generate large errors. Weighted least-squares methods are not effective, because all distances from stencil points to the face center are similar.

To improve the accuracy of gradient reconstruction, a general approximate mapping (AM) method is proposed. The AM method is motivated by the observation that, in an exactly mapped coordinate system (e.g., in polar coordinates for grids generated around a circle), gradient approximation for a radial function is as good as the gradient approximation in domains with no curvature. The AM method described next is a second-order approximation to the exact mapping.

The AM method constructs a local mapping based on the distance function that supplies the distance from a field point to designated boundaries and is readily available in practical codes. In this paper, we use the exact distance function defined at the cell centers. A more practical alternative (not used here) is to define the distance function at the grid nodes. The least-squares minimization is applied in a local coordinate system (ξ, η), where η is the coordinate normal to the boundary, and ξ is the coordinate parallel to the boundary. Figure 14 illustrates construction of the local coordinates. The vector normal to the boundary is constructed at the face center μ as an average of two normal vectors defined at the cell centers across the face. The corresponding unit vector $\hat{\mathbf{n}}_\mu$ is defined as

$$\hat{\mathbf{n}}_\mu = \frac{\mathbf{r}_A - \mathbf{r}_A^* + \mathbf{r}_B - \mathbf{r}_B^*}{|\mathbf{r}_A - \mathbf{r}_A^* + \mathbf{r}_B - \mathbf{r}_B^*|} \tag{25}$$

where $\mathbf{r}_A$ and $\mathbf{r}_B$ are the positions of the control-volume centers, and $\mathbf{r}_A^*$ and $\mathbf{r}_B^*$ are the corresponding positions of the closest boundary points. The distance to the boundary at the face center μ is approximated as

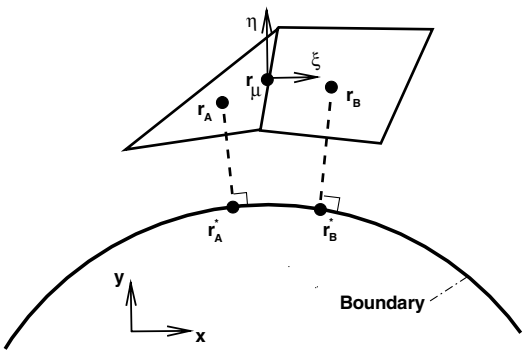

Fig. 14 Sketch of coordinate system used in AM method.

Table 3 High-Γ grids: relative errors of gradient reconstruction

	I	II	III	IV
NC	$O(h_\theta^2)$	$O(h_\theta)$	$O(h_\theta)$	$O(h_\theta)$
CC–NN	$O(h_\theta^2)$	$O(1)$	$O(1)$	$O(1)$
CC–NN–AM	$O(h_\theta^2)$	$O(h_\theta^2)$	$O(h_\theta)$	$O(h_\theta)$
CC–CS	$O(h_\theta^2)$	$O(h_\theta^2)$	$O(h_\theta^2)$	$O(1)$
CC–NA	$O(h_\theta^2)$	$O(h_\theta^2)$	$O(\mathcal{A}h_\theta)$	$O(\mathcal{A}h_\theta)$
CC–NA–AM	$O(h_\theta^2)$	$O(h_\theta^2)$	$O(h_\theta)$	$O(h_\theta)$

$$s_\mu = \frac{|\mathbf{r}_A - \mathbf{r}_A^*| + |\mathbf{r}_B - \mathbf{r}_B^*|}{2} \tag{26}$$

The unit vector normal to $\hat{\mathbf{n}}_\mu$ is denoted as $\hat{\tau}_\mu$. For constructing the least-squares minimization at a control-volume face with the center $\mathbf{r}_\mu$, each stencil point P is mapped onto the local coordinates $(\xi_P,\ \eta_P)$ by

$$\xi_P = (\mathbf{r}_P - \mathbf{r}_\mu) \cdot \hat{\tau}_\mu \tag{27}$$

$$\eta_P = s_P - s_\mu \tag{28}$$

where $s_P = |\mathbf{r}_P - \mathbf{r}_P^*|$.

The gradient approximation accuracy for a radial function on high-Γ grids of types I–IV from the previous study [24], supplemented with the CC–CS and CC–NA–AM results, is summarized in Table 3. Convergence of the maximum gradient errors over all faces is tabulated. Note that large $O(\mathcal{A}h_\theta)$ relative errors for the CC–NA scheme occur on high-Γ grids of type III at only the radially oriented faces in the gradient component tangential to the face; the errors at other faces and in the gradient component normal to the radial face are small.

B. Discretization-Error Convergence

Discretization errors of CC schemes are compared with the errors of the NC scheme on refined stretched high-Γ grids of types III and IV. The tests are performed for the manufactured solution $U = \sin(5\pi r)$. The computational grids (see Fig. 13) are derived from background regular cylindrical grids with a radial extent of $1 \le r \le 1.2$ and an angular extent of 20 deg. The background grids have four times more nodes in the radial direction than in the circumferential direction. The grid-refinement study is performed on grids stretched in the radial direction, with a fixed maximal aspect ratio of $\mathcal{A} \approx 1000$. The maximal value of parameter Γ changes approximately from 24 to 3. The stretching ratio is changing as $\beta = 1.25, 1.11, 1.06$, and 1.03.

Convergence of the L_1 norms of the discretization errors on grids of type III is shown in Fig. 15a. All tests have been performed stochastically. The plot symbols again indicate the mean errors, and bars indicate the maximum and minimum errors observed on each scale. As expected, error variations observed on grids of the same scale due to stochastic grid irregularities are small for all schemes and decreasing for smaller scales (larger number of degrees of freedom). The errors of the NC, CC–NA, CC–CS, CC–NN–AM, and CC–NA–AM solutions converge with second order and are almost overplotted on fine grids, indicating the same accuracy per degree of freedom. The errors of the CC–NN scheme are significantly higher and converge with first order.

Convergence of the L_1 norms of the discretization errors on grids of type IV, shown in Fig. 15b, is similar to the results in Fig. 15a. The effective mesh sizes of CC and NC formulations are much closer on mixed grids than on triangular grids. The CC–CS scheme is omitted because, on mixed-element grids, its current version is similar to the CC–NN scheme. Note also that the CC–NA scheme may lose stability on high-Γ mixed-element grids. On these grids, there are topologies for which the node solution is averaged from four neighboring cells. The four cell centers involved in such averaging may be located on a straight line, thus leading to degeneration. In

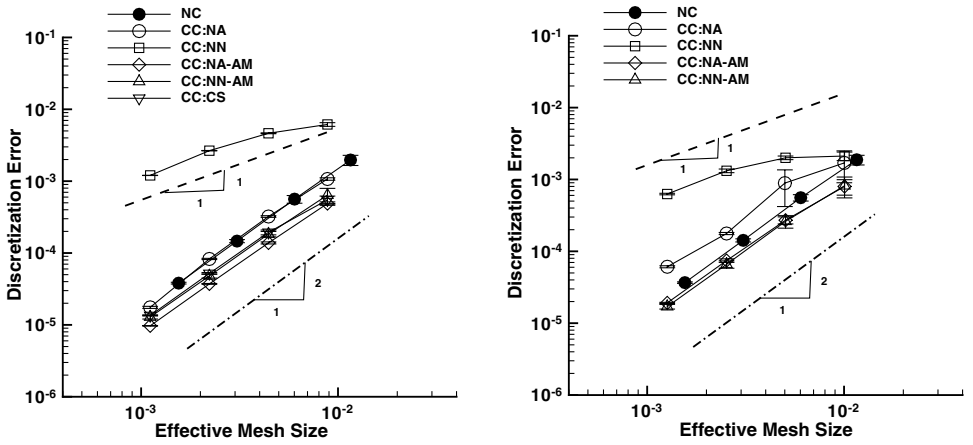

a) Convergence on grids of type III b) Convergence on grids of type IV

Fig. 15 Convergence of the L_1 norms of the discretization errors on high-Γ grids.

these (rare) instances, large negative contributions appear on the main diagonals of the full linearization matrix. The scheme may still be solved and even provide a reasonable accuracy. The AM version of the CC–NA scheme, CC–NA–AM, is always stable. Overall, discretization errors of the NC scheme and the best CC schemes (CC–CS, CC–NN–AM, and CC–NA–AM) converge with second order, are insensitive to grid irregularities, and are comparable at an equivalent number of degrees of freedom.

IX. Conclusions

Complexity and accuracy of NC and CC FVDs have been compared for Poisson's equation as a model of viscous fluxes. Considering complexity, the NC scheme has the lowest complexity (i.e., its stencil involves the least number of degrees of freedom). The CC schemes using least-squares face-gradient reconstruction, the CC–NN and the CC–CS schemes, have complexity comparable with that of the NC scheme. Complexity of the CC–NA scheme is the highest.

The accuracy comparisons have been made for two classes of tests. The first class is representative of adaptive-grid simulations and involves irregular grids in rectangular geometries. The second class is representative of high-Reynolds number turbulent flow simulations over a curved body and involves highly stretched grids, typical of those generated by the method of advancing layers. All tests have been performed for smooth manufactured solutions on consistently refined grids. Grid perturbations and stretching have been intentionally introduced independently of solution variation to bring out the worst possible behavior.

For the tests of the first class, only the CC–NA scheme with clipping can fail to approximate gradients and/or to converge to the exact solution. However, note that the clipping is introduced mainly for stability of the inviscid solution and can be avoided for the viscous terms. All other schemes demonstrate similar qualities:

1) The discretization errors converge with second order and are quantitatively similar on grids of the same type with equivalent degrees of freedom. On high-aspect-ratio randomly perturbed grids, discretization errors for all schemes are orders of magnitude higher than corresponding errors on unperturbed grids.

2) Gradient reconstruction may produce $O(\mathcal{A}h_x)$ large relative errors on grids of types I_p–IV_p, where $\mathcal{A}$ is the grid aspect ratio and h_x is the larger mesh spacing.

3) Truncation errors do not converge, as expected.

For the tests of the second class, the range of grid parameters has been chosen to enforce significant curvature-induced grid deformations, characterized by parameter Γ. These high-Γ tests proved to be more discriminating:

1) The discretization errors are small and converge with second order for the NC scheme, for approximate mapping schemes (CC–NN–AM and CC–NA–AM), for the CC–NA scheme, and for the CC–CS scheme on triangular grids. The CC–NN scheme without approximate mapping shows first-order convergence and the highest level of discretization errors.

2) Accurate gradient reconstruction is provided by the NC scheme and the CC–NN–AM and CC–NA–AM schemes on all grids and by the CC–CS scheme on triangular grids. On high-Γ grids of types II–IV, the CC–NN scheme without approximate mapping generates $O(1)$ errors in gradient reconstruction. The CC–NA scheme may produce large relative gradient errors proportional to the product of the grid aspect ratio and the larger mesh spacing.

3) Without AM, the CC–NA scheme may degenerate on mixed grids.

The major conclusion is that the accuracy and complexity of the NC and the best CC schemes on irregular grids are comparable at equivalent number of degrees of freedom.

X. Acknowledgment

This paper was supported by the NASA Fundamental Aeronautics Program, Supersonics Project, NASA Research Announcement contract NNL07AA23C, with N. K. Yamaleev as the principal investigator.

Appendix A: Node-Centered Discretization on Grids of Types II and III in Rectangular Geometries

In this section, we show that the NC discretization of the Laplacian is equivalent to the standard finite-difference formula for arbitrary aspect-ratio grids of types II and III in rectangular geometry. Consider a set $\{T_j\}$ of triangles/tetrahedra that share a node j. For the NC scheme, the Green–Gauss gradient within each cell is given by

$$\overline{\nabla U}^{\,T} = \frac{1}{D\Omega^T} \sum_{i\in\{i^T\}} U_i \check{\mathbf{n}}_i \tag{A1}$$

where D is the number of spatial dimensions, $D = 2$ for triangles, $D = 3$ for tetrahedra, Ω^T is the volume of cell T, $\{i^T\}$ is a set of nodes of the cell T, and $\check{\mathbf{n}}_i$ is the inward-directed area vector of the face opposite to the node i. Then, the NC discretization (or equivalently, the standard Galerkin discretization) of the Laplacian at j is defined as

$$\int_\Omega \Delta U \,\mathrm{d}\Omega = \int_{\partial\Omega} \nabla U \cdot \mathbf{n} = -\sum_{T\in\{T_j\}} \frac{1}{D^2\Omega^T} \sum_{i\in\{i^T\}} U_i(\check{\mathbf{n}}_i \cdot \check{\mathbf{n}}_j^T) \tag{A2}$$

where Ω is the dual control volume around j and $\check{\mathbf{n}}_j^T$ is the inward-directed area vector opposite to node j in cell T. The right-hand side of Eq. (A2) can be separated into two terms:

$$\int_\Omega \Delta U \,\mathrm{d}\Omega = -\frac{1}{D^2}\sum_{T\in\{T_j\}}\left(\frac{\check{\mathbf{n}}_j^T\cdot\check{\mathbf{n}}_j^T}{\Omega^T}\right)U_j - \frac{1}{D^2}\sum_{T\in\{T_j\}}\sum_{i\in\{i^T\},i\neq j}\left(\frac{\check{\mathbf{n}}_i\cdot\check{\mathbf{n}}_j^T}{\Omega^T}\right)U_i \tag{A3}$$

The first term contains contributions from the node value U_j, and the second term contains contributions from the neighbors.

For general 2-D triangular grids (Fig. A1),

$$\int_\Omega \Delta U \,\mathrm{d}\Omega = -\frac{1}{4}\sum_{T\in\{T_j\}}\left(\frac{\check{\mathbf{n}}_j^T\cdot\check{\mathbf{n}}_j^T}{\Omega^T}\right)U_j - \frac{1}{4}\sum_{k\in\{k_j\}}\left(\frac{\check{\mathbf{n}}_k^L\cdot\check{\mathbf{n}}_j^L}{\Omega^L}+\frac{\check{\mathbf{n}}_k^R\cdot\check{\mathbf{n}}_j^R}{\Omega^R}\right)U_k \tag{A4}$$

where $\{k_j\}$ is a set of neighbors of j, and the normals are inward normals, as defined in Fig. A1. This can be written also in terms of angles between edges,

$$\int_\Omega \Delta U \,\mathrm{d}\Omega = -\frac{1}{4}\sum_{T\in\{T_j\}}\left(\frac{\check{\mathbf{n}}_j^T\cdot\check{\mathbf{n}}_j^T}{\Omega^T}\right)U_j + \frac{1}{2}\sum_{k\in\{k_j\}}(\cot\theta^L+\cot\theta^R)U_k \tag{A5}$$

which is often used to show that the discretization is positive for triangulations with $\theta^L+\theta^R<\pi$. Consider now a grid of type III, shown in Fig. A2, which is constructed by inserting diagonals into a Cartesian grid. For this particular diagonal splitting, node 3 does not contribute to the discretization equation (A4), because it is not a neighbor to node j, and nodes 1, 5, and 7 do not contribute, because the angles θ^L and θ^R are both 90 deg; therefore, the coefficient $(\cot\theta^L+\cot\theta^R)$ vanishes. This is, in fact, true for any diagonal splittings: contributions from the corner nodes 1, 3, 5, and 7 are always zero, either because it is not in the actual stencil or because the coefficient vanishes. Observe also that angles θ^L and θ^R for other nodes are independent of the diagonal splitting; thus, we always have

$$\cot\theta^L=\cot\theta^R=\begin{cases}\frac{h_y}{h_x} & \text{for nodes 2 and 6}\\ \frac{h_x}{h_y} & \text{for nodes 4 and 8}\end{cases} \tag{A6}$$

Moreover, it is easy to show that the coefficient of U_0 is also independent of the splitting. Hence, the discretization equation (A4) can be written, for arbitrary splittings, as

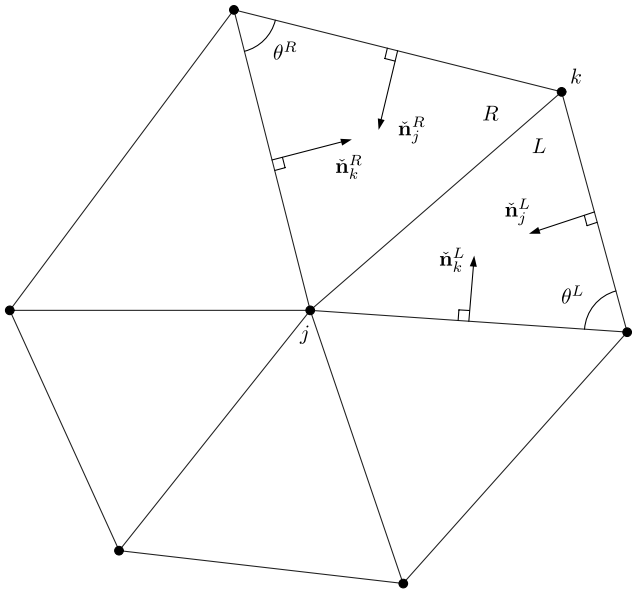

Fig. A1 NC stencil on triangular grids. Note that the normals are not scaled.

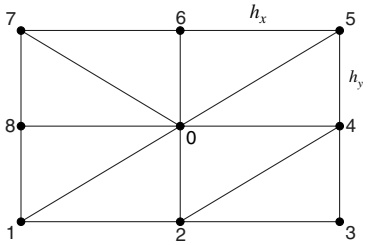

Fig. A2 Triangular grid with arbitrary aspect ratio.

$$\int_\Omega \Delta U \,\mathrm{d}\Omega = -2\left(\frac{h_x}{h_y}+\frac{h_y}{h_x}\right)U_0+\frac{h_y}{h_x}U_2+\frac{h_x}{h_y}U_4+\frac{h_y}{h_x}U_6+\frac{h_x}{h_y}U_8 \tag{A7}$$

$$= h_xh_y\left(\frac{U_4-2U_0+U_8}{h_x^2}+\frac{U_6-2U_0+U_2}{h_y^2}\right) \tag{A8}$$

This is a common five-point finite-difference discretization. Therefore, the NC scheme on grids of types II and III with the arbitrary aspect ratio is equivalent to the common five-point Laplacian. For stretched grids, the corner nodes still do not contribute to the discretization. A similar property holds in 3-D, for which the NC scheme on a tetrahedral grid derived from a (stretched) Cartesian grid by arbitrary diagonal splitting is equivalent to a common seven-point finite-difference discretization.

References

[1] Thomas, J. L., Diskin, B., and Rumsey, C. L., "Towards Verification of Unstructured-Grid Solvers," *AIAA Journal*, Vol. 46, No. 12, Dec. 2008, pp. 3070–3079. doi:10.2514/1.36655

[2] Haselbacher, A. C., "A Grid-Transparent Numerical Method for Compressible Viscous Flow on Mixed Unstructured Meshes," Ph.D. Thesis, Loughborough Univ., Loughborough, Leicestershire, U.K., 1999.

[3] Haselbacher, A. C., McGuirk, J. J., and Page, G. J., "Finite-Volume Discretization Aspects for Viscous Flows on Mixed Unstructured Grids," *AIAA Journal*, Vol. 37, No. 2, 1999, pp. 177–184. doi:10.2514/2.711

[4] Thomas, J. L., Diskin, B., and Nishikawa, H., "A Critical Study of Agglomerated Multigrid Methods for Diffusion on Highly-Stretched Grids," *Computers and Fluids* (accepted for publication).

[5] Holmes, D. G., and Connell, S. D., "Solution of the 2-D Navier–Stokes Equations on Unstructured Adaptive Grids," 9th AIAA CFD Conference, AIAA Paper 89-1392, June 1989.

[6] Rausch, R. D., Batina, J. T., and Yang, H. T., "Spatial Adaptation Procedures on Unstructured Meshes for Accurate Unsteady Aerodynamic Flow Computation," 9th AIAA CFD Conference, AIAA Paper 89-1392, June 1989.

[7] Frink, N. T., "Assesment of an Unstructured-Grid Method For Predicting 3-D Turbulent Viscous Flows," 34th AIAA Aerospace Science Meeting and Exhibit, AIAA Paper 96-0292, Jan. 1996.

[8] Haselbacher, A. C., "On Constrained Reconstruction Operators," 44th AIAA Aerospace Science Meeting and Exhibit, AIAA Paper 2006-1274, Jan. 2006.

[9] Barth, T. J., "Numerical Aspects of Computing High-Reynolds Number Flow on Unstructured Meshes," 29th AIAA Aerospace Science Meeting, AIAA Paper 91-0721, Jan. 1991.

[10] Coirier, W. J., "An Adaptively-Refined, Cartesian, Cell-Based Scheme for the Euler and Navier–Stokes Equations," NASA TM 106754, Oct. 1994.

[11] Frink, N. T., "Tetrahedral Unstructured Navier–Stokes Methods for Turbulent Flows," *AIAA Journal*, Vol. 36, No. 11, 1998, pp. 1975–1982. doi:10.2514/2.324

[12] Mavriplis, D. J., "Revisiting the Least-Square Procedure for Gradient Reconstruction on unstructured Meshes," 18th AIAA CFD Conference, AIAA Paper 2003-3986, June 2003.

[13] Petrovskaya, N. V., "The Choice of Weight Coefficients for Least-Square Gradient Approximation," *Journal of Mathematical Modeling*, Vol. 16, No. 5, 2004, pp. 83–93 (in Russian).

[14] Smith, T. M., Barone, M. F., Bond, R. B., Lorber, A. A., and Baur, D. G., "Comparison of Reconstruction Techniques for Unstructured Mesh Vertex Centered Finite Volume Scheme," 18th AIAA CFD Conference, AIAA Paper 2007-3958, June 2007.

[15] Anderson, W. K., and Bonhaus, D. L., "An Implicit Upwind Algorithm for Computing Turbulent Flows on Unstructured Grids," *Computers and Fluids*, Vol. 23, No. 1, 1994, pp. 1–21. doi:10.1016/0045-7930(94)90023-X

[16] Diskin, B., and Thomas, J. L., "Accuracy Analysis for Mixed-Element Finite-Volume Discretization Schemes," National Institute of Aerospace TR 2007-08, Hampton, VA, Aug. 2007.

[17] Hirsch, C., *Numerical Computation of Internal and External Flows. Vol. 1, Fundumentals Of Numerical Discretization*, Wiley, New York, 1988.

[18] Syrakos, A., and Goulas, A., "Estimate of the Truncation Error of Finite Volume Discretization of the Navier–Stokes Equations on Collocated Grids," *International Journal for Numerical Methods in Fluids*, Vol. 50, No. 1, 2006, pp. 103–130. doi:10.1002/fld.1038

[19] Turkel, E., "Accuracy of Schemes with Nonuniform Meshes for Compressible Fluid Flows," *Applied Numerical Mathematics*, Vol. 2, No. 6, 1986, pp. 529–550. doi:10.1016/0168-9274(86)90006-1

[20] Giles, M. B., "Accuracy of Node-Based Solutions on Irregular Meshes," *11th International Conference on Numerical Methods in Fluid Dynamics*, edited by D. L. Dwoyer, M. Y. Hussaini, and R. Voigt, Vol. 323, Lecture Notes in Physics, Springer–Verlag, New York, 1989, pp. 369–373.

[21] Forsyth, P. A., and Sammon, P. H., "Quadratic Convergence for Cell-Centered Grids," *Applied Numerical Mathematics*, Vol. 4, No. 5, 1988, pp. 377–394. doi:10.1016/0168-9274(88)90016-5

[22] Kreiss, H. O., Manteuffel, T. A., Wendroff, B., and White, A. B., "Supra-Convergence Schemes on Irregular Grids," *Mathematics of Computations*, Vol. 47, No. 176, Oct. 1986, pp. 537–554.

[23] Manteuffel, T. A., and White, A. B., "The Numerical Solution of the Second-Order Boundary Value Problem on Nonuniform Meshes," *Mathematics of Computations*, Vol. 47, No. 176, Oct. 1986, pp. 511–536.

[24] Diskin, B., and Thomas, J. L., "Accuracy of Gradient Reconstruction on Grids with High Aspect Ratio," National Institute of Aerospace TR 2008-12, Dec. 2008.

[25] Diskin, B., Thomas, J. L., Nielsen, E. J., Nishikawa, H., and White, J. A., "Comparison of Node-Centered and Cell-Centered Unstructured Finite-Volume Discretizations. Part 1: Viscous Fluxes," 47th AIAA Aerospace Science Meeting, AIAA Paper 2009-597, 2009.

Z. J. Wang
Associate Editor